Instability of an electron-plasma shear layer in an externally imposed strain flow

N. C. Hurst,[1, a)] J. R. Danielson,[1] D. H. E. Dubin,[1] and C. M. Surko[1]

Department of Physics, University of California San Diego, 9500 Gilman Drive, La Jolla, California 92093, USA

The $\mathbf{E} \times \mathbf{B}$ shear instability of a two-dimensional (2D) filament (i.e., a thin, rectangular strip perpendicular to the magnetic field) of magnetized pure electron plasma is investigated experimentally in the presence of an externally imposed strain flow. Data are acquired using a specialized Penning-Malmberg trap in which strain flows can be applied in 2D by biasing segmented electrodes surrounding the plasma. The $\mathbf{E} \times \mathbf{B}$ drift dynamics are well-described by the Drift-Poisson equations, which are isomorphic to the 2D Euler equations describing ideal fluids. Thus, the experimental results correspond to the Rayleigh instability of a shear layer in a 2D ideal fluid, where the electron density is analogous to the fluid vorticity. Shear layers are prepared by stretching initially axisymmetric electron vortices using a strong, applied strain flow. The data at early times are in quantitative agreement with a linear model which extends Rayleigh's work to account for the influence of an external strain flow. In the presence of weak strain, the system approximately maintains a phase relationship that corresponds to an instantaneous Rayleigh eigenmode. The instability develops into the nonlinear regime later in time and at smaller spatial scales as the strain rate is increased. A secondary vortex pairing instability is observed, but it is suppressed when the strain-to-vorticity ratio exceeds roughly 0.025. In this way, vorticity transport perpendicular to the filament is diminished due to the applied strain.

I. INTRODUCTION

Shear flows can be found in a wide variety of quasi-two-dimensional (2D) plasma and fluid systems, both naturally occurring and human-made, across a broad range of scales. In many cases, shear instabilities give rise to turbulence and transport, often with important consequences. A few common examples include shear flows and zonal flows in geophysical fluids (e.g., atmospheres and oceans),[1–4] magnetically confined fusion plasmas,[5–7] accretion and protoplanetary disks,[8–10] and non-neutral plasmas.[11–16] Thus, understanding the stability properties of shear layers is a key objective in plasma and fluid research. Often, the stability and persistence of shear flows is attributed to external conditions such as planetary rotation, topography, or background density gradients.[1,4,6,8] In contrast, it is well known that isolated shear flows in 2D, inviscid, incompressible (ideal) fluids are unstable.[17,18]

The linear stability of an infinitesimally thin, 2D inviscid shear layer with a density discontinuity was first studied by Kelvin and Helmholtz,[18] whose names are now commonly used to refer to a broad class of shear instabilities. Rayleigh generalized their results to account for finite layer width in a uniform density (incompressible) fluid, showing that a piecewise linear flow velocity profile is unstable for wavenumbers ranging from zero to roughly the inverse layer width.[3,17] More recent work has focused on smooth flow profiles,[19–21] nonlinear physics,[22–24] and 3D effects.[4,25] However, in many physically realistic sit-

uations, shear layers are embedded in complicated (perhaps turbulent) background flow fields.[26–29] Thus, they are often subjected to shear and strain flows which are sourced externally by other nearby flow structures. This situation was studied theoretically and numerically by Dritschel, et. al.,[30,31] showing that the external flow could significantly modify the stability properties of the shear layer.

Here, experiments with single component electron plasmas are used to study the Rayleigh instability on a thin filament of vorticity, and the effect of external strain flow on the wave growth and saturation is explored. Further, several effects due to the applied strain are identified that contribute to limiting the spreading of the vorticity that results from the instability.

The experiments described here take advantage of an analogy between the $\mathbf{E} \times \mathbf{B}$ guiding center drift dynamics of non-neutral pure electron plasmas and the dynamics of 2D ideal fluids, where the electron density plays the role of fluid vorticity.[32] A specially designed Penning-Malmberg plasma trap is used in which the electron fluids are subjected to externally applied $\mathbf{E} \times \mathbf{B}$ strain flows by differentially biasing a segmented electrode surrounding the plasma, a technique which has been used recently to study dynamical behavior of elliptical vortices.[33–35] We focus here on the influence of external strain on the stability properties of shear layers in a 2D ideal fluid. The shear layers are created by stretching initially axisymmetric electron vortices into thin filamentary structures in the plane perpendicular to the magnetic field using strong external strain flows.[33,36] Subsequently, the applied strain is either removed or reduced so as to study the resulting Rayleigh instability of the filaments. The behavior is characterized by the strain to vorticity ratio $\epsilon^* \equiv \epsilon/\omega_0$, where the strain rate ϵ is proportional

---

a)E-mail: nhurst@wisc.edu; Present address: Department of Physics, University of Wisconsin - Madison.

to the magnitude of an applied quadrupolar potential, ω_0 is the magnitude of the peak (central) vorticity, and $0 \leq \epsilon^* \leq 0.045$ in the present work. Interestingly, while the strain rates considered here have a profound impact on the instability, they are significantly smaller than that required for destabilization of an elliptical vortex, $\epsilon^* \sim 0.15$.[35,37]

We find that at early times, the plasma behavior is well described by a simple, linear model in which the vorticity is treated as piecewise constant inside the layer.[31] This model generalizes Rayleigh's analysis to include a background strain flow, resulting in non-modal behavior where the waves experience temporary amplification while they are stretched toward low wavenumber. The data show that, for the range of strain rates studied here, the coupled waves on the upper and lower surface of the layer approximately maintain a phase relationship that corresponds to an instantaneous Rayleigh eigenmode which changes in time due to the strain. Although the experimental procedure offers little or no control over the initial wave spectrum, the data suggest that the waves may be growing from discrete-particle or finite gyroradius fluctuations at a scale three orders of magnitude smaller than the initial layer width.

If the wave amplification is sufficient, nonlinearity becomes important and the instability saturates due to wave breaking and vortex formation. A key result is that saturation occurs at later times and at smaller scales as the strain rate is increased. A secondary vortex pairing instability[24,38] is observed in which vortices enter into pairwise orbits and eventually merge, however the instability is suppressed for $\epsilon^* \gtrsim 0.025$ since the vortices are advected apart faster than the pairing rate. Thus, the applied strain flow has the effect of significantly reducing transport perpendicular to the filament, such that spreading of electron vorticity due to the instability is less than the spatial extent of the initial filament for $\epsilon^* \gtrsim 0.04$. For $\epsilon^* \sim 0.045$, the spatial scale of the vortices approaches the resolution of the diagnostic, and so no firm conclusions can be made regarding vortex suppression or stabilization of the filament.

This paper is organized in the following way: details of the experimental procedure are given in Sec. II; the linear theory and corresponding data are presented in Sec. III; and in Sec. IV, data are presented regarding the nonlinear regime of the instability. Finally, in Sec. V, the results are discussed and conclusions are given.

II. EXPERIMENTAL METHODS

A. The analogy between electron plasmas and 2D fluids

Plasmas with nonzero charge density and macroscopic electric fields are often referred to as non-neutral plasmas, or single-component plasmas if only one species is present. They exhibit a variety of interesting behavior[39] and they arise in important applications such as ac-

celerator beams[40] and antimatter experiments.[41] The work presented here is based on the result that the $\mathbf{E} \times \mathbf{B}$ guiding-center drift dynamics of magnetized, single-component plasmas can mimic the behavior of 2D ideal fluids.[11,32] Such experiments are typically performed using pure electron plasmas in a Penning-Malmberg trap, a device in which radial confinement is achieved using a strong, uniform, applied axial magnetic field $\mathbf{B} = -B\hat{\mathbf{z}}$, and axial confinement is achieved by creating an electrostatic potential well $\phi(z)$ using a set of hollow, cylindrical electrodes surrounding the plasma.[39,42]

Electrons inside the trap bounce axially between potential barriers at frequency $f_b = \bar{v}/2L$ where $\bar{v} = (k_B T/m)^{\frac{1}{2}}$ is the thermal velocity, k_B is Boltzmann's constant, T is the plasma temperature, m is the electron mass, and L is the plasma length (SI units). In the plane perpendicular to $\mathbf{B}$, they execute cyclotron orbits of frequency $f_g = eB/m$ and spatial scale given by the gyroradius $r_g = \bar{v}/f_g$, as well as $\mathbf{E} \times \mathbf{B}$ drift motion at a characteristic "vortex" frequency scale $f_v = en/4\pi B\epsilon_0$, where n is the electron density, e is the electron charge, and ϵ_0 is the permittivity of free space. Like-particle electron collisions occur at a frequency given roughly by $f_c \sim n\bar{v}d^2$, where d is the classical distance of closest approach.[43] When the frequency scales are separated as

$$f_g \gg f_b \gg f_v \gg f_c, \qquad (1)$$

the cyclotron motion and the bounce motion can be time-averaged and the electrons treated as thin cylinders of charge which drift in the (x, y) plane inside the trap without collisional dissipation.

Under these conditions, the drift dynamics are given by the Drift-Poisson equations

$$\left(\frac{\partial}{\partial t} - \frac{\nabla\phi \times \hat{\mathbf{z}}}{B} \cdot \nabla\right)n = 0; \ \nabla^2\phi = -\frac{en}{\epsilon_0}, \qquad (2)$$

where $\phi(x, y)$ is the electric potential in 2D and $\mathbf{v} = -\nabla\phi \times \hat{\mathbf{z}}/B$ is the $\mathbf{E} \times \mathbf{B}$ drift velocity.[32] Equations (2) are isomorphic to the 2D Euler equations describing ideal fluid

$$\left(\frac{\partial}{\partial t} - \nabla\psi \times \hat{\mathbf{z}} \cdot \nabla\right)\omega = 0; \ \nabla^2\psi = \omega, \qquad (3)$$

where ψ is the fluid stream function, $\mathbf{v} = -\nabla\psi \times \hat{\mathbf{z}}$ is the flow velocity, and $\omega = \nabla \times \mathbf{v}$ is the fluid vorticity. Therefore, the electron density is the analog of the fluid vorticity, and the electric potential is the analog of the fluid stream function under the transformations $\omega \to en/\epsilon_0 B$ and $\psi \to \phi/B$.[32] The individual electrons are analogous to point vortices with circulation $e/BL\varepsilon_0$ and core size equal to the gyroradius r_g, and so $\omega \geq 0$ in these experiments.[44] Due to this correspondence, electron plasmas can be used to study 2D ideal fluids in the laboratory in a way which is inaccessible to traditional fluid experiments (e.g., water tanks) due to viscous and/or three-dimensional (3D) effects. The plasma system offers additional advantages including direct, high-resolution diagnosis of the vorticity field using a phosphor screen and

CCD camera,[45] and precise electrical control over the initial conditions and boundary conditions.[34,46–48] Furthermore, experimental parameters can be varied rapidly in a way which is difficult to accomplish using numerical simulations.

The 2D ideal fluid system described by Eqs. (3) offers an important and simple setting for basic studies of nonlinear fluid phenomena including self-organization, structure formation, and turbulence.[49,50] It can be described as an infinite-dimensional Hamiltonian system where the spatial coordinates serve as canonical variables.[51] Variants of Eqs. (3) have been used extensively to model a variety of important flows in geophysics, astrophysics, and plasma physics.[1,2,4,8,52,53]

The vorticity plays an important role in that, along with the boundary conditions, it uniquely determines the instantaneous flow field through the Poisson equation. Vorticity and strain are mathematical counterparts: the vorticity is the magnitude of the (imaginary) eigenvalues of the antisymmetric part of the velocity gradient tensor $\frac{1}{2}(\nabla\mathbf{v} - \nabla\mathbf{v}^{\mathrm{T}})$, and it is associated with elliptical flow geometry and rotational fluid motion; whereas the strain rate is the magnitude of the (real) eigenvalues of the symmetric part $\frac{1}{2}(\nabla\mathbf{v}+\nabla\mathbf{v}^{\mathrm{T}})$, and it is associated with hyperbolic geometry and stretching motion. The dynamics of 2D ideal fluids are characterized by a tendency of the vorticity to arrange itself into rotating clumps known generally as vortices. When isolated, these structures are typically axisymmetric and stable, whereas in the presence of external flows (e.g., due to other vortices or boundaries) they can be destabilized and stretched into thin filaments or shear layers.[33,35,36,54,55]

B. The eight-segment trap apparatus

The experiments presented here are conducted using pure electron plasmas confined in a Penning-Malmberg trap apparatus which is engineered specifically to study 2D ideal fluid dynamics subject to external flows. The apparatus and experimental technique are discussed in detail elsewhere,[34,35] and so only a brief description is given here. The apparatus is referred to as the eight-segment trap (8ST) since its key feature is an electrode extending over the length of the plasma which is segmented azimuthally into eight pieces that can be electrically biased independently. In this way, the boundary conditions of the fluid system can be controlled precisely in 2D, allowing for the imposition of externally imposed flows which advect the trapped electrons due to the $\mathbf{E}\times\mathbf{B}$ drift.

The 8ST electrode structure is depicted schematically in Fig. 1(a), including an electron gun (left) and a diagnostic consisting of a phosphor screen and CCD camera (right). Electrodes I, III, and V are solid (not segmented) and are typically biased to $V_c = -100$ V in order to axially confine the electrons. Electrode II is the eight-segment electrode in which the fluid experiments take
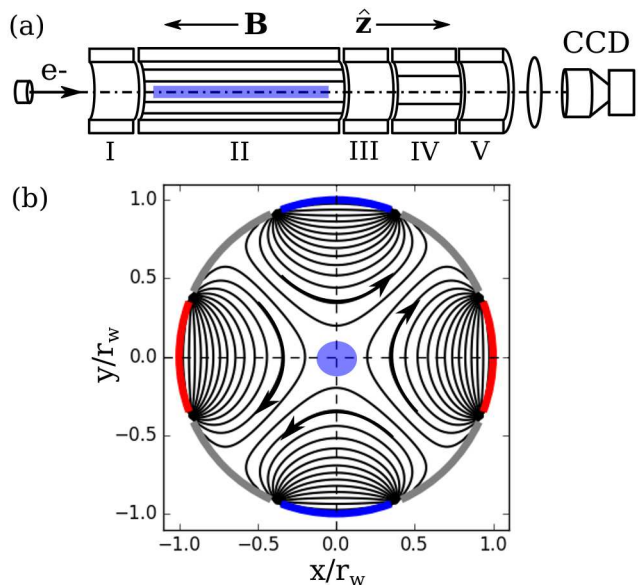

FIG. 1. A schematic diagram of the eight-segment trap apparatus. (a) The electrode structure, consisting of solid electrodes I, III, and V, the eight-segment electrode II, and a four-segment electrode IV. Also shown are an electron gun (left) and a diagnostic consisting of a phosphor screen and CCD camera (right). (b) A cross-section of electrode II including streamlines (black) of an external strain flow created by biasing the segments to voltages $(V_s, 0, -V_s, 0, V_s, 0, -V_s, 0)$ beginning along the positive $x-$axis. Positive (negative) voltages are shown as red (blue), arrows indicate the flow direction, and the initial plasma is depicted as a blue circle.

place, and electrode IV is a shorter electrode with four segments which is used to condition the electron density profile $n(r)$ using the rotating wall technique.[48,56,57] The entire structure is immersed in an axial magnetic field $B = 4.8$ T and held at ultra-high vacuum conditions at pressure $\sim 10^{-9}$ Torr. The inner radius of the electrodes is $r_w = 13$ mm, the length of the entire electrode structure is 440 mm, and the length of electrode II is 260 mm.

The plasmas studied here are described by particle number $N = 4.93 \times 10^8$, peak density $n_0 = 1.19 \times 10^{14}$ m^{-3} (corresponding to peak vorticity $\omega_0 = 450$ krad/s), length $L \approx 240$ mm, radius $r_v = 2.3$ mm and temperature $T \sim 0.1$ eV. The corresponding frequency scales are $f_g = 134$ GHz, $f_b \approx 276$ kHz, $f_v \sim 36$ kHz, and $f_c \sim 3$ kHz, and so the scale separation (1) is satisfied to at least an order of magnitude.

Externally imposed $\mathbf{E} \times \mathbf{B}$ flows are generated by electrically biasing the segments of electrode II, which amounts to specifying the fluid stream function on the boundary $\psi(r_w, \theta)$. Here, we focus on a quadrupolar configuration in which the segments are biased to voltages $(V_s, 0, -V_s, 0, V_s, 0, -V_s, 0)$, beginning with the segment along the positive $x-$axis, as shown in Fig. 1(b). Also shown are contours of the electric potential (i.e., streamlines of the external flow) which are given by a series solu-

tion to the Laplace equation. Near the origin ($r/r_w \ll 1$), the second-order term in the potential expansion is dominant, and so the external flow field is given approximately by

$$\psi_s = \frac{1}{2}\epsilon(x^2 - y^2); \quad \mathbf{v_s} = \epsilon(y\hat{\mathbf{x}} + x\hat{\mathbf{y}}), \qquad (4)$$

which is called a simple strain flow, where

$$\epsilon = \frac{1.8 V_s}{B r_w^2} \qquad (5)$$

is the strain rate, and the strain axis (i.e., the orientation of the positive eigenvector) is given by $y = x$. The next lowest nonzero term in the potential expansion is sixth-order and therefore negligible for $r/r_w \lesssim 0.5$.

The plasma dynamics can deviate from Eqs. (2) due to violations of the scaling (1) or perturbative 3D effects.[34,58] These deviations include collisional viscous diffusion on long timescales $\gtrsim 1$ ms,[44,59] slow magnetron drifts due to the curvature of the endcap potentials at frequency ~ 150 Hz,[25,58] and flow dissipation and/or smearing of vorticity features at spatial scales approaching the gyroradius $r_g = 0.16$ μm or the interparticle spacing $(n_0 L)^{-\frac{1}{2}} = 0.19$ μm. The former two processes are expected to be unimportant in this work since the experiments take place over < 150 μs. However, the vorticity filaments studied here can be stretched rapidly to small scales at which discrete-particle and gyroradius effects may be relevant, although these scales cannot be resolved with the CCD diagnostic.

C. Experimental procedure and data collection

The experiments consist of a series of run cycles, each of duration 10-20 seconds, which proceed as follows. First, plasmas are generated by the scattering of electrons from the gun into an electrostatic potential well between electrodes I and V. They are then radially compressed using the rotating wall technique, where a rotating electric field is applied using electrode IV.[48,56,57] This results in an axisymmetric, quasi-flat density distribution that can be approximated by

$$n(r) = n_0 \exp\left[-\left(\frac{r}{r_v} \right)^\alpha \right], \qquad (6)$$

where $\alpha \sim 10$ is called the "smoothness parameter." The plasmas are then confined between electrodes I and III and the $m = 1$ diocotron mode[40] is damped using a feedback circuit, thus positioning the density centroid at the origin. Finally, the plasmas are allowed to cool *via* cyclotron radiation in the strong magnetic field.[60] At this point, they have the necessary properties for the fluid experiment. A CCD measurement of the vorticity distribution $\omega(x, y)$ at this time is shown in Fig. 2(a). The radial vorticity profile $\omega(r) = (2\pi)^{-1} \int \omega(r, \theta) d\theta$ is shown in Fig. 2(b) along with a least-squares fit to Eq. (6),
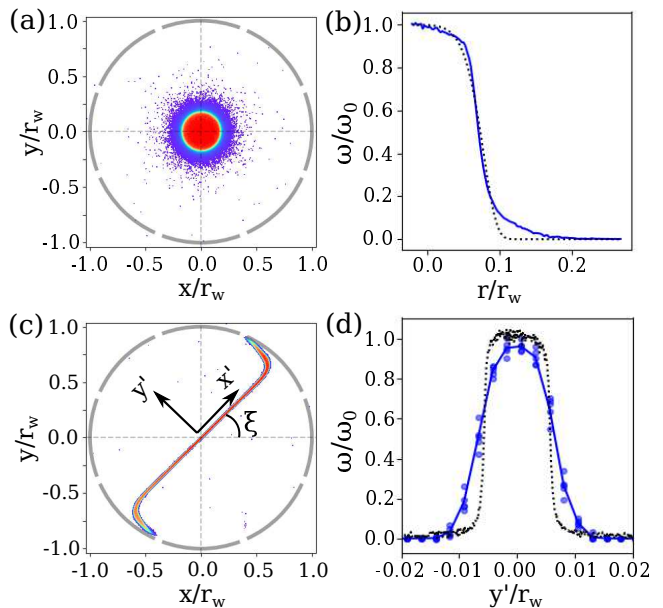

FIG. 2. Measurements of the initial vortex and filament used in the experiments. (a) CCD image of the initial axisymmetric vortex just prior to application of the strain flow, where data are truncated for $\omega < 0.03\omega_0$; (b) radial vorticity profile $\omega(r)$ (blue) corresponding to panel (a), along with a fit to Eq. (6) (dotted); (c) CCD image of the initial filament following application of a strong external strain flow, with the filament angle ξ and filament-aligned coordinate system (x', y') indicated; and (d) cross-section of the filament as measured by the CCD (blue), and that obtained by scaling the profile in panel (b) according to Eq. (7) (black).

yielding the aforementioned values of ω_0, r_v, and α. The profile closely resembles a step function, except for an extended, low-vorticity tail near the edge of the distribution.

Next, the axisymmetric vortex is stretched into a thin filament using a strong external strain flow. The segments of electrode II are biased as described above with strain-to-vorticity ratio $\epsilon^* = 0.377$ for a time interval $\Delta t^* \equiv \omega_0 \Delta t = 9$. Here, ϵ^* is sufficiently large that the vortex behaves passively and distorts elliptically with aspect ratio

$$\lambda = a/b = \exp(2\epsilon t), \qquad (7)$$

where a and b are the semimajor and semiminor axes, $d(ab)/dt = 0$ due to incompressibility, and the ellipse orientation ξ is close to that of the strain axis.[36] When $a \sim r_w$, the filament curves at the ends due to higher-order terms in the potential expansion, and electrons are advected out of the system through gaps between the segments of electrode II. For $\lambda \gg 1$ the geometry can be regarded as rectangular, and we refer to the distribution as a filament of thickness $2b$. From Fig. 2, the procedure described above yields $2b_0 = 0.155$ mm ($r_v/b_0 \sim 30$), which serves as the initial condition for the shear instability experiment.
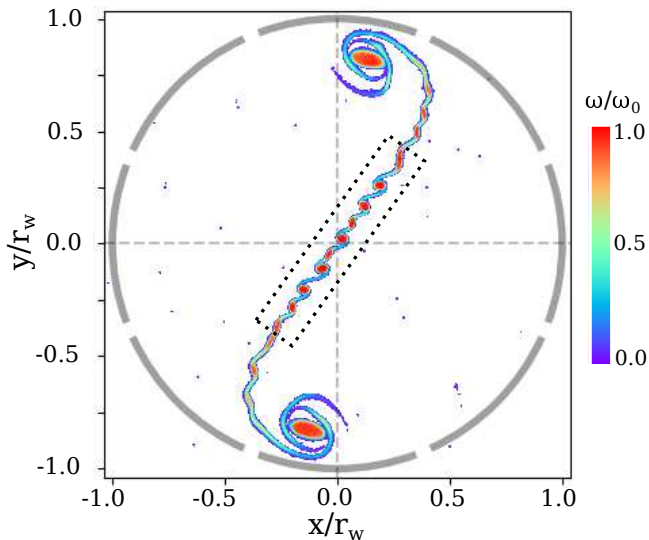
FIG. 3. An example CCD measurement of vorticity data (color map) of a filament undergoing shear instability in the absence of strain ($\epsilon^* = 0$) at time $t^* = 33.75$. Also shown is a region of interest (dotted) of width r_w and height $0.2r_w$ in which the analysis presented in Sec. III and IV is conducted.

At $t = 0$ the strain rate is reduced either to $\epsilon^* = 0$ or to some intermediate value $0.005 \leq \epsilon^* \leq 0.045$. The filament is allowed to evolve for a time t, after which the vorticity is diagnosed destructively by grounding electrode III, accelerating the electrons onto a phosphor screen biased to $+5$ kV and recording the fluorescent light with the CCD camera. The pixel size is 32.5 μm, and the signal-to-noise ratio (at peak vorticity) is typically $\sim 10^2$. Experimental uncertainty is determined by repeating each measurement five times. The surface roughness of the initial filament is much smaller than the pixel size, and so it cannot be measured directly.

D. Data analysis techniques

A CCD image of the initial filament at $t = 0$ is given in Fig. 2(c). We define a coordinate frame (x', y') where the $x'-$axis is aligned with the filament at an angle ξ with respect to the $x-$axis. The expected filament profile $\omega(y')$ is obtained by scaling the cross-section of the initial vortex [cf. Fig. 2(a)] by a factor $\exp(-\epsilon\Delta t)$ [cf. Eq. (7)]. It is plotted in Fig. 2(d) along with the measured profile through the origin $\omega(x' = 0, y')$ [e.g., obtained from the CCD image in Fig. 2(c)]. The measured profile is smoothed due to convolution with the discrete-pixel grid of the CCD camera. The measured peak gradient is $\max(\partial\omega/\partial y') = 4.58 \times 10^6$ rad/mm-s whereas the actual value is likely close to the prediction 20×10^6 rad/mm-s based on Eq. (7).

A sample CCD image of the vorticity is given in Fig. 3 at $t^* \equiv \omega_0 t = 33.75$ for $\epsilon^* = 0$ (in the absence of external strain). Here, the shear instability near the origin
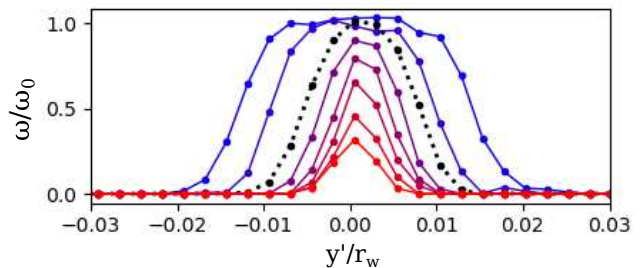

FIG. 4. Measurements of the filament profile $\omega(x' = 0, y')$ for the initial vortex [cf. Fig. 2(a,b)] subjected to an external strain flow with $\epsilon^* = 0.377$ for time intervals $\Delta t^* = 7.2 - 13.5$ (blue to red). The initial filament used in the experiments ($\Delta t^* = 9$) is shown as a dotted line, and circles indicate pixel locations.

has developed into an array of discrete vortex structures. Furthermore, two larger vortices have developed near the boundary at either end of the filament. These structures form early relative to those near the origin due to the curvature of the intial filament near the boundary as well as image charges which generate a cooperative shear flow (i.e., a background fluid rotation in the same sense as the vorticity). In order to avoid image effects, higher-order terms in the applied flow, and the influence of the vortices near the boundary, we restrict our analysis to the region $(-0.5 \leq x' \leq 0.5, -0.1 \leq y' \leq 0.1)$, which is indicated by a dotted box in Fig. 3. At lowest order, the vortices near the boundary are expected to contribute a superposed strain flow with strain rate $\epsilon^* \sim 0.005$ where the axis is inclined by about $-30°$ relative to the filament.

When $\epsilon^* \gtrsim 0.01$, electrons near the boundary are removed from the system through small gaps between the segments of electrode II, and so the boundary vortices do not form. However, in some cases these electrons can orbit the biased electrode segment and return into the trap volume through an adjacent gap.[34] Although this behavior is not completely understood, the number of re-entrant electrons is typically small ($< 0.01N$), and so they have little effect on the instability of the filament near the origin.

The instability causes vorticity transport in the direction perpendicular to the filament, leading to a broader flow profile with lower mean shear. This is quantified by the root-mean-square spread of vorticity perpendicular to the initial filament, or the effective filament half-width

$$b_{\text{eff}} = \left[\Gamma^{-1} \int \omega y'^2 \mathrm{d}A\right]^{\frac{1}{2}}, \qquad (8)$$

where $\Gamma = \int \omega \mathrm{d}A$ is the total circulation and $\mathrm{d}A = \mathrm{d}x\mathrm{d}y$ is an area element.

When the filament thickness approaches the pixel size, the CCD signal decreases due to convolution with the pixel grid. This places a limit on the spatial scale of vorticity features that can be diagnosed. This is demonstrated in Fig. 4, which shows measurements of the filament profile $\omega(x' = 0, y')$ when the initial vortex [cf.
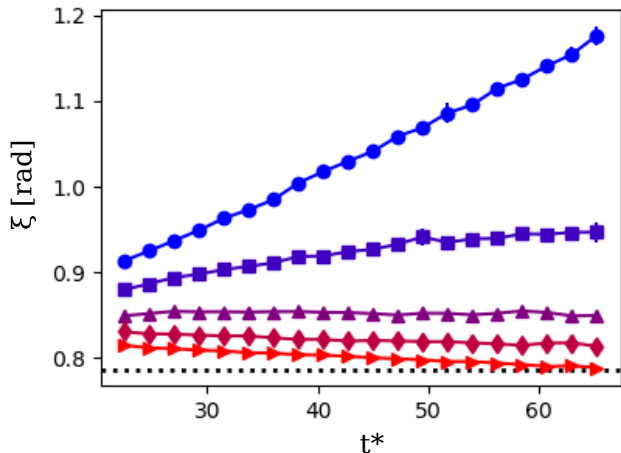
FIG. 5. Measurements of the evolution of the filament angle near the origin, calculated using Eq. (9), for $\epsilon^* = 0$ (blue circles), 0.01 (squares), 0.02 (triangles), 0.03 (diamonds), and 0.04 (red triangles). The orientation of the strain axis $\pi/4$ is also shown (dotted). Note that most of the error bars here are obscured by the data markers.

Fig. 2(a,b)] is subjected to an external strain flow with $\epsilon^* = 0.377$ for times $\Delta t^* = 7.2 - 13.5$. The initial condition used for the experiments, corresponding to $\Delta t^* = 9$, is shown as a dotted line.

Since the initial filament is closely aligned with the strain axis, $\xi(t = 0) \approx \pi/4$. However, in general ξ changes with time as the filament rotates, depending on the external strain rate. The angle of the filament ξ is found by calculating quadrupole moments $Q_{ij} = \Gamma^{-1} \int \omega(x, y)(2x_i x_j - r^2 \delta_{ij}) \mathrm{d}A$ of the vorticity distribution for $r/r_w < 0.5$, where δ_{ij} is the Kronecker delta function. The angle is given by

$$\xi = \frac{1}{2} \tan^{-1}\left(\frac{Q_{xy}}{Q_{xx}}\right). \tag{9}$$

Figure 5 shows measurements of $\xi(t)$ for a few different values of ϵ^*. In the absence of strain, the filament rotates continuously since the total circulation is nonzero, and ξ is irrelevant due to rotational symmetry of the boundary. For nonzero strain, the filament may rotate toward or away from the strain axis depending on the value of ϵ^*. However, the rate of rotation $\mathrm{d}\xi/\mathrm{d}t$ is slow compared to that of the instability. For the data presented here (for $\epsilon^* \neq 0$), the maximum angle reached between the strain axis and the filament is $\xi - \pi/4 \approx 12°$ for $\epsilon^* = 0.005$, $t^* = 65.25$. Thus, for simplicity and convenience, it is assumed in the following analysis that the filament is always aligned with the strain axis.

III. LINEAR INSTABILITY

A. Theoretical model

The linear theory of a piecewise strip of vorticity was studied by Rayleigh[3,17] as a generalization of the Kelvin-Helmholtz mechanism to a finite-thickness shear layer in an ideal (constant-density) fluid. Later, Dritschel, et. al.[30,31] extended this analysis to consider the influence of external shear and strain flows on the instability. Here, the vorticity is taken to be a constant ω_0 between the upper and lower boundaries and zero elsewhere, a technique known as contour dynamics.[18] In this model, waves propagate on the upper and lower surface of the layer and their evolution is coupled, which can lead to phase-locking and instability.[3,61] Following Dritschel,[31] the boundaries of the filament subject to a perturbation with wavenumber k in the x' direction are defined according to

$$y'_{\pm} = 2b\left(\pm\frac{1}{2} + \eta_{\pm}\right) \tag{10}$$

and

$$\eta_{\pm}(t) = \mathrm{Re}[\tilde{\eta}_{\pm}(t) \exp(ikx')], \tag{11}$$

where $\tilde{\eta}_{\pm}$ is the complex wave amplitude. The linear evolution of the waves on the upper and lower surface is described by the coupled equations

$$i\frac{\mathrm{d}\tilde{\eta}_{\pm}}{\mathrm{d}t^*} = \pm\frac{1}{2}(1 - 2bk)\tilde{\eta}_{\pm} \mp \frac{1}{2}\exp(-2bk)\tilde{\eta}_{\mp}. \tag{12}$$

In the absence of strain, the wavenumber and the filament thickness are constant in time, $k = k_0$ and $b = b_0$, where k_0 is the initial wavenumber of a perturbation. In this case, Eqs. (12) describe the Rayleigh shear instability, yielding unstable eigenmodes for wavenumbers in the range $0 < 2bk < 2bk_c \approx 1.278$. The normalized growth rate is

$$\gamma^* \equiv \gamma/\omega_0 = \frac{1}{2}[\exp(-4bk) - (1 - 2bk)^2]^{\frac{1}{2}}, \tag{13}$$

which has a single maximum $\gamma_m^* \approx 0.201$ at $2bk_m \approx 0.797$. The eigenmodes are normal modes in which the waves on the upper and lower surface have equal amplitude and are phase-shifted by an angle

$$\Phi = \cos^{-1}[(1 - 2bk)\exp(2bk)]. \tag{14}$$

When Eq. (14) is not satisfied, the wave growth is modified and the instability is non-modal (does not grow exponentially). Furthermore, the phase-locked state acts as an attractor in that waves initialized with arbitrary Φ will rapidly (over a few t^*) approach the eigenmode solution where Eq. (14) is satisfied.[61] For large k, the wave interactions are weakened due to the exponential coupling term in Eq. (12). For $k > k_c$, the coupling is too weak to maintain phase-locking and so the system is
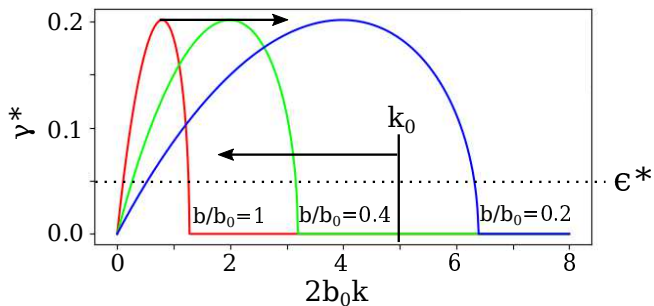
FIG. 6. Schematic diagram of shear-layer instability with a background strain flow. Colored curves show the Rayleigh growth rate [cf. Eq. (13)] for $b/b_0 = 1$, 0.4, and 0.2, where b decreases over time as per Eq. (15). A perturbation with initial wavenumber $2b_0k_0 = 5$ is also indicated, where k decreases over time as per Eq. (16). The horizontal dashed line indicates the strain rate $\epsilon^* = 0.05$; in regions of high and low k where this value exceeds the Rayleigh growth rate, waves are stabilized directly due to the strain.

marginally stable and the two waves travel in opposite directions.

In the presence of an applied strain flow defined by Eq. (4), and assuming that the filament remains aligned with the strain axis, the instability is described by Eqs. (10-12) where the filament half-thickness and wavenumber evolve over time due to the strain as[31]

$$b = b_0 \exp(-\epsilon t), \tag{15}$$

$$k = k_0 \exp(-\epsilon t). \tag{16}$$

The former effect can be understood as filament thinning due to inflow perpendicular to the strain axis, and the latter as wave stretching due to outflow parallel to the strain axis. Due to these time-dependent parameters, the dynamics of Eqs. (12) are generally non-modal. Analytic solutions have not been obtained, and so they are studied numerically. The overall result is that waves experience temporary amplification while k is near k_m, before becoming damped as $k \to 0$ due to the filament thinning effect, which directly opposes wave growth.[31] Furthermore, initially stable waves with $k_0 > k_c$ are destabilized over time as b and k decrease.

This behavior is depicted schematically in Fig. 6, where the colored curves show the Rayleigh growth rate, Eq. (13), for different values of b. Here and throughout the rest of this work, wavenumbers are normalized to the initial filament thickness $2b_0$. Since b decreases over time, the unstable region expands toward high k, as shown by the rightward arrow. A perturbation with initial wavenumber $2b_0k_0 = 5$ is also shown, where a leftward arrow indicates that the wave is stretched toward low k over time due to the strain. Finally, a horizontal dashed line indicates that the stability threshold is raised due to direct damping associated with the filament thinning effect at the strain rate ϵ^* (shown here as 0.05), and
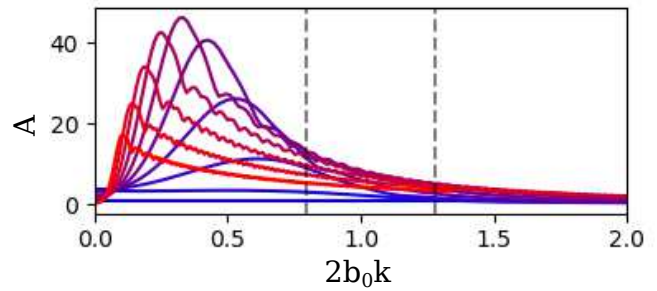

FIG. 7. Wave slope amplification spectrum $A(k)$ over time $t^* = 0 - 50$ (blue to red) for $\epsilon^* = 0.03$. Dashed lines indicate $2b_0k_m = 0.797$ and $2b_0k_c = 1.278$.

so regions of weak growth at low and high k are stabilized.

In addition to direct wave damping at low k, the applied strain modifies wave growth by changing the eigenmode phase relationship due to filament thinning. In this way, the attracting, phase-locked state given by Eq. (14) acts as a "moving target" toward which the system continuously evolves. However, when the strain is sufficiently small, the system approaches the phase-locked state faster than it changes, and so the linear evolution can be regarded approximately as a continuous series of instantaneous Rayleigh eigenmodes.

Theoretical analysis in the long-wavelength limit shows that the filament is completely stabilized (i.e., all perturbations are damped) for $\epsilon^* \geq 0.25$,[31] which is much higher than the range of strain rates studied here. However, in the linear picture all waves are eventually damped at low k, and so a useful question is whether a given wave is amplified sufficiently so that nonlinear effects become important. Following Dritschel,[31] nonlinearity is expected when the wave slope exceeds unity,

$$s \equiv \left[\left(\frac{\partial y'_+}{\partial x'} \right)^2 + \left(\frac{\partial y'_-}{\partial x'} \right)^2 \right]^{\frac{1}{2}} > 1. \tag{17}$$

Amplification of the mean wave slope is described by $\langle s(t) \rangle = A(t) \langle s(t = 0) \rangle$ where

$$A(t) = \exp(-2\epsilon t) \left[\frac{|\tilde{\eta}_+(t)|^2 + |\tilde{\eta}_-(t)|^2}{|\tilde{\eta}_+(0)|^2 + |\tilde{\eta}_-(0)|^2} \right]^{\frac{1}{2}} \tag{18}$$

is the amplification factor with $A(t = 0) = 1$ by definition, and $\langle \cdot \rangle$ indicates a spatial average over the wave period.[31] An example of the evolution $A(k,t)$ averaged over initial phase is shown in Fig. 7 for $\epsilon^* = 0.03$. Here, the amplification at early times (blue curves) is small and peaked close to k_m. As time proceeds (purple curve) the peak has grown and shifted to a lower value of k. At later times (red curves), as the peak moves to progressively smaller values of k, the amplification reaches a maximum and then decreases, showing that at late times the amplification eventually goes to zero, and the waves

are damped. The small variations of $A(k)$ appear to be an artifact related to the phase-averaging technique.

B. Experimental data

In this section, small-amplitude waves growing at early times on the surface of the electron filament are diagnosed and compared to the linear contour dynamics model discussed above.[3,17,31] The vorticity data inside the region of interest $(-0.5 \leq x'/r_w \leq 0.5, -0.1 \leq y'/r_w \leq 0.1)$ are reduced to two separate lines $y'_\pm(x')$ by numerically determining the maximum and minimum of $\partial\omega/\partial y'$ as a function of x'. This approach breaks down when the wave slope (17) becomes infinite, and so it is useful only in the linear and weakly nonlinear regimes. In this section, the experimental analysis concerns a spectrum of unstable waves growing on the electron filament, as opposed to the linear model described above in which waves are treated independently. Thus, waves can break unevenly across the filament, and so rather than averaging the wave slope over x',[31] fulfillment of the criterion (17) at any point x' is interpreted as a departure from the global linear description.

Measurements of the early evolution of $\omega(x', y')$, $y'_\pm(x')$, and $s(x')$ are given in Fig. 8 for $\epsilon^* = 0$, $t^* = 22.5$, 24.75, 27, and in Fig. 9 for $\epsilon^* = 0.02$, $t^* = 22.5$, 27, 31.5, where time proceeds from left to right. The transition to nonlinearity, as defined by Eq. (17), occurs between the second and third panel in both cases, and so the third panel corresponds to the weakly nonlinear regime (i.e., prior to wave breaking). These data indicate that wave growth is delayed in the presence of applied strain. For $\epsilon^* \neq 0$ (cf. Fig. 9), the filament thickness decreases somewhat due to the strain prior to observable growth of the instability. This leads to a reduction in the CCD signal, as described above with regard to Fig. 4.

Figure 10 shows spectra obtained from experimental measurements of $y'_\pm$ for $\epsilon^* =$ (a) 0, (b) 0.01, (c) 0.02, and (d) 0.03. The solid lines and shaded areas indicate the average and standard deviation of five identical runs. The experimental spectra of the upper and lower contours are found by taking the fast Fourier transform (FFT) of the surface perturbations normalized to the initial filament thickness

$$\tilde{y}'_\pm = (y'_\pm - \langle y'_\pm \rangle)/2b_0, \tag{19}$$

where the average is performed along x' and the normalization factor of 400 pixels is included in the inverse FFT. The spectra from the upper and lower layer are then added in quadrature to obtain a measure of the total wave amplitude,

$$|\tilde{y}'| = (|\tilde{y}'_+|^2 + |\tilde{y}'_-|^2)^{\frac{1}{2}}. \tag{20}$$

The measured difference between $|\tilde{y}'_+|$ and $|\tilde{y}'_-|$ is typically $< 5\%$, which is expected when the two surfaces approximately satisfy the phase relationship of Eq. (14).

The data are compared to solutions of Eqs. (10)-(12) (dotted) where b and k evolve according to Eqs. (15) and (16), and the model spectra are calculated as $|\tilde{y}'| = \exp(-\epsilon t)(|\tilde{\eta}_+|^2 + |\tilde{\eta}_-|^2)^{\frac{1}{2}}$. Since the initial perturbation amplitudes $\Delta y'_\pm(t = 0)$ are unknown, the solutions are averaged over the initial phase $\Phi(t = 0)$ and fit to the data in the linear regime by choosing the initial condition $|\tilde{y}'(t = 0)| = 0.5$ (independent of k and ϵ^*).

The experimental data and model predictions shown in Fig. 10 are in close quantitative agreement. The data and model both show the transfer of wave power toward low k as ϵ^* increases, consistent with the wave stretching mechanism discussed above. Following the transition to nonlinearity, weak spectral power is observed at high k due to wave-wave interactions. Whether or not the apparent variations in the data at intervals $2b_0\Delta k \sim 0.1$ are of physical significance is presently unknown.

By performing an inverse FFT, the initial condition $|\tilde{y}'(t = 0)| = 0.5$ yields the surface roughness $\Delta y'_\pm = 2.5 \times 10^{-3}b_0 = 0.194$ μm. Thus, the amplitude of the seed waves from which the instability grows is comparable to both the interparticle spacing (0.19 μm) and the gyroradius (0.16 μm), suggesting that these non-fluid effects could be responsible for development of the instability. It is remarkable that the techniques described in Sec. II for preparing the initial filament result in such a smooth surface. In order to determine whether the waves grow due to (density-dependent) discrete-particle effects, filaments were studied with peak vorticity ranging from 293 to 563 krad/s. However, no clear variation of seed wave amplitude with density was observed. In principle one could look for finite-gyroradius effects by varying B, however in practice it is difficult to do this without changing other aspects of the experimental procedure, and so this was not attempted. Therefore, the source of the initial perturbations remains unknown.

The FFT routine provides phase information for each k on the upper and lower surfaces of the filament. The phase differences $\Phi(k)$ are plotted in Fig. 11 for (a) $\epsilon^* = 0$ at times $t^* = 22.5$, 24.75, 27 (proceeding left to right), and (b) $\epsilon^* = 0.02$, $t^* = 22.5$, 27, 31.5. They are compared to numerical solutions of Eqs. (12) averaged over initial phase. They are also compared to the phase relationship (14) for the instantaneous Rayleigh eigenmode, where k is scaled by $\exp(\epsilon t)$ so as to offset the change in b. In row (a), the data compare favorably to Eq. (14) and to the numerical model, suggesting that the growing waves are consistent with the unstable eigenmodes studied by Rayleigh. For $k > k_c$, the phase is expected to be random since the Rayleigh theory predicts counter-propagating waves on the two surfaces, which is apparent in the experimental data and numerical solutions.

In Fig. 11(b), it can be observed that the reduction in b due to the applied strain leads to phase-locking and therefore instability at higher k, even though the amplitude remains fairly low (see the data in Fig. 10). The data and model are roughly in agreement at low
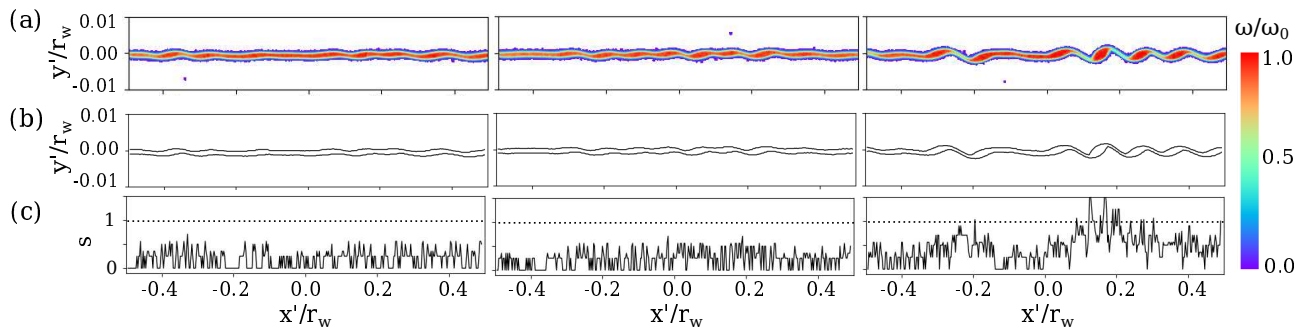
FIG. 8. Measurements of (a) the vorticity ω (color map), (b) the upper and lower filament boundaries $y'_\pm$, and (c) the wave slope s given by Eq. (17), for $\epsilon^* = 0$ at times $t^* = 22.5, 24.75, 27$ (left to right).
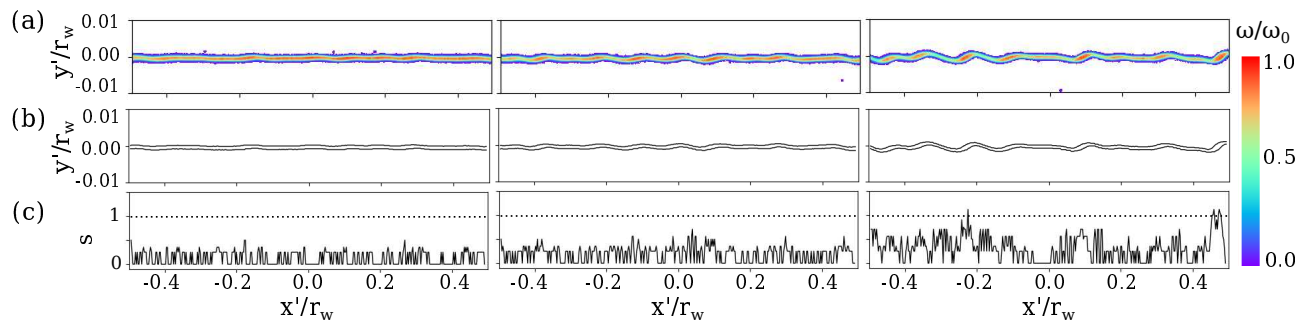

FIG. 9. Measurements of (a) the vorticity ω (color map), (b) the upper and lower filament boundaries $y'_\pm$, and (c) the wave slope s given by Eq. (17) for $\epsilon^* = 0.02$ at times $t^* = 22.5, 27, 31.5$ (left to right).

k, however they diverge from the eigenmode phase curve near the instability threshold at $k \lesssim k_c \exp(\epsilon t)$, likely due to the finite time required for a recently destabilized wave to phase-lock. It is anticipated that higher values of strain will result in greater departures from the eigenmode state, until the phase becomes completely unlocked and wave growth is inhibited.

To summarize this section, the $\mathbf{E} \times \mathbf{B}$ shear instability of the electron filaments has been measured in the linear regime with and without an applied strain flow. In the absence of strain, wave growth is observed across a wide range of the spectrum between $k = 0$ and k_c. In the presence of strain, spectral transfer toward low k is observed due to wave stretching, and waves are destabilized over time at higher wavenumbers $k > k_c$ as the filament thins. Moreover, for small values of strain the two surface waves appear to approximately maintain a phase shift which corresponds to an instanaeous Rayleigh eigenmode. These measurements were compared to a linear contour dynamics model,[31] and shown to be in good quantitative agreement.

IV. NONLINEAR REGIME

In this section, results are presented regarding the nonlinear behavior of the instability at late times. An overview of the dynamics is given in Fig. 12, where vor-

ticity data are shown for $\epsilon^* =$ (a) 0, (b) 0.015, (c) 0.03, and (d) 0.045 at times $t^* = 22.5, 33.75, 45$, and 56.25 (left to right). In the absence of external strain, unstable waves grow and eventually break, and the instability saturates due to the formation of discrete, rotating vortex structures. The resulting linear array of vortices is then subject to a secondary vortex pairing instability, in which neighboring vortices enter into pairwise orbits and may eventually merge.[24,38] This behavior can be observed in the last two panels of Fig. 12(a), where merger events result in the formation of larger-scale vortex structures.

In the presence of strain, the filament thinning and wave stretching mechanisms cause the instability to develop later in time and saturate at smaller spatial scales as ϵ^* increases. Evidence of vortex pairing can be observed for $\epsilon^* = 0.015$ in Fig. 12(b), however, for $\epsilon^* = 0.03$ [row (c)] the vortices are advected away from one another due to the strain rapidly enough that the pairing instability is suppressed. For $\epsilon^* = 0.045$ [row (d)], the filament width approaches the pixel size by the time the instability develops, and so detailed study of the resulting vortices is not possible. The last panel in row (c) is enlarged in Fig. 13, showing evidence that small-scale vortices do indeed form at $\epsilon^* = 0.045$. Thus, due to limitations imposed by the CCD pixel resolution, vortex suppression due to the strain has not been observed here. It remains an open question what value of ϵ^* is sufficient to prevent vortex formation or nonlinear behavior altogether, although this
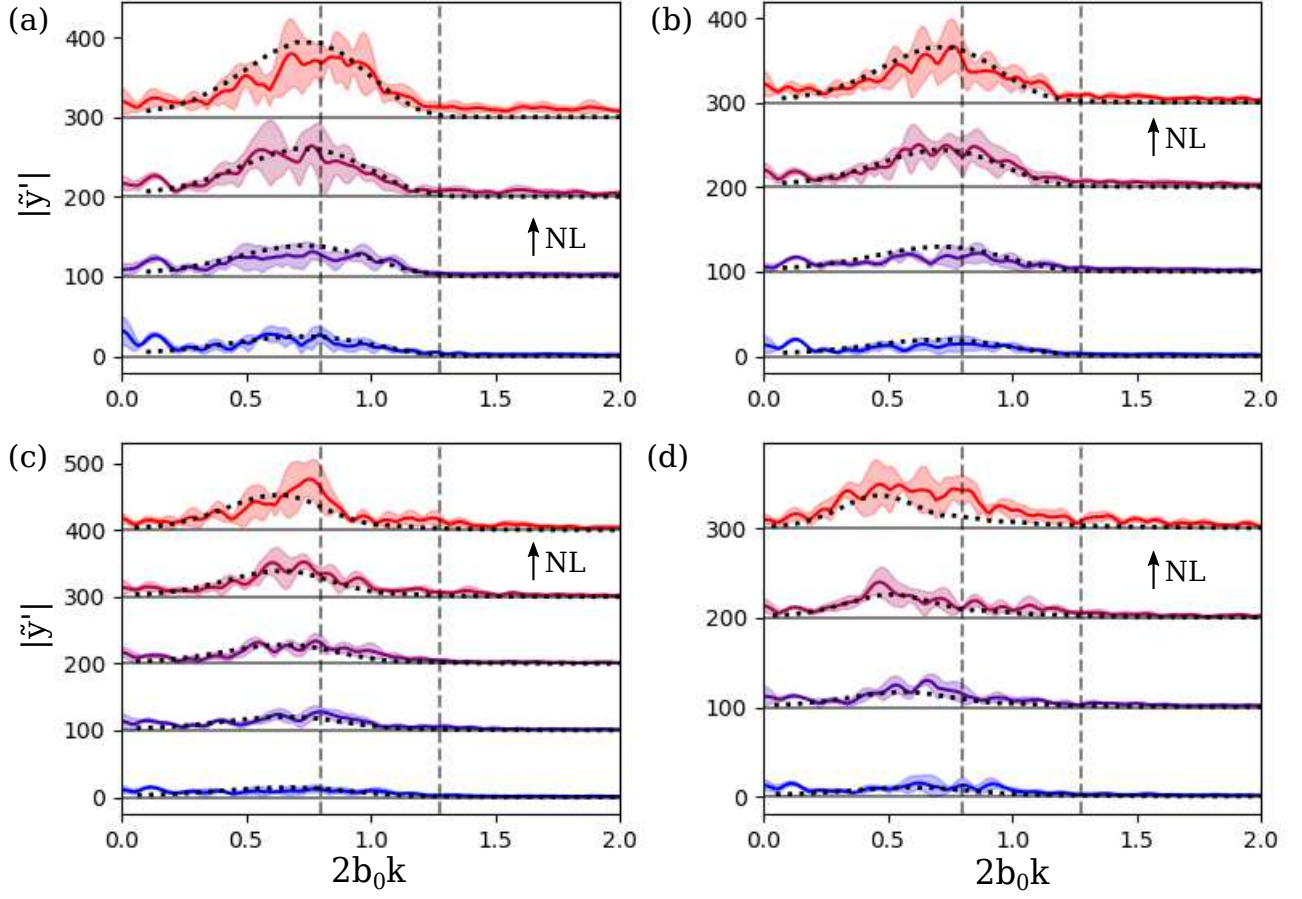
FIG. 10. Experimental wave spectra $|\tilde{y}'|$ [cf. Eq. (20)] are compared to predictions of a contour dynamics model described by Eqs. (12) (dotted) for (a) $\epsilon^* = 0$, $t^* = 22.5, 24.75, 27, 29.25$; (b) $\epsilon^* = 0.01$, $t^* = 22.5, 24.75, 27, 29.25$; (c) $\epsilon^* = 0.02$, $t^* = 22.5, 24.75, 27, 29.25, 31.5$; (d) $\epsilon^* = 0.03$, $t^* = 22.5, 27, 31.5, 36$. Time proceeds upwards in each panel from blue to red, separated for clarity by intervals of $\Delta|\tilde{y}'| = 100$. The nonlinear transition [cf. Eq. (17)] is indicated (NL), as are k_m and k_c (dashed lines). Shaded regions indicate the experimental uncertainty.

likely depends on the initial seed wave amplitude.

The progression of the instability in the nonlinear regime can also be visualized using the perpendicular vorticity spread b_{eff} normalized to its initial value, as described in Sec. II, Eq. (8). This is shown in Fig. 14 for ϵ^* ranging from 0 to 0.045. As before, the data points and error bars are given by the average and standard deviation of five identical runs. Black circles indicate the onset of nonlinearity [i.e., the first data point at which the wave slope surpasses unity, as defined by Eq. (17)]. For smaller values of ϵ^*, quasi-exponential growth is observed at early times. Following the onset of nonlinearity, b_{eff} levels off and a plateau is observed, which corresponds to primary vortex formation (this is especially pronounced for $\epsilon^* = 0$). After this, a secondary increase in b_{eff} is observed due to the vortex pairing mechanism. For $\epsilon^* \gtrsim 0.025$, no significant secondary increase is observed, indicating that the pairing instability has been suppressed due to the applied strain. Thus, the transport of vorticity perpendicular to the filament due to the instability is significantly reduced as ϵ^* is increased. For

$\epsilon^* = 0.045$, b_{eff} is close to the pixel size and so the results may not be reliable.

The vortex pairing instability can be described in a simple way using a point-vortex model in which the vortices are perturbed with respect to an infinite linear array. If the vortices are assumed to be patch-like with area A and are separated evenly by a distance Δ, then disturbances grow exponentially at a rate $\sigma = \pi\omega_0 A/4\Delta^2$.[18] Inspection of Fig. 12(a) (second panel) yields $A \approx 0.21$ mm^2 and $\Delta \approx 1.3$ mm, and so $\sigma/\omega_0 \approx 0.1$, which is greater than the strain rates studied here. However, as the strain is increased, the primary vortices form with larger separation and less circulation. For example, in Fig. 12(c) (last panel), $A \approx 0.08$ mm^2, $\Delta \approx 5.2$ mm, and so $\sigma/\omega_0 \approx 0.024$, which is smaller than ϵ^* and therefore consistent with suppression of the pairing instability.

The tendency of the instability to saturate at later times and at smaller scales as ϵ^* increases is evident in Fig. 14. This trend is quantified further in Fig. 15, which shows how the saturation time and spatial scale vary with the applied strain. Panel (a) shows the time t^*_{NL} at which
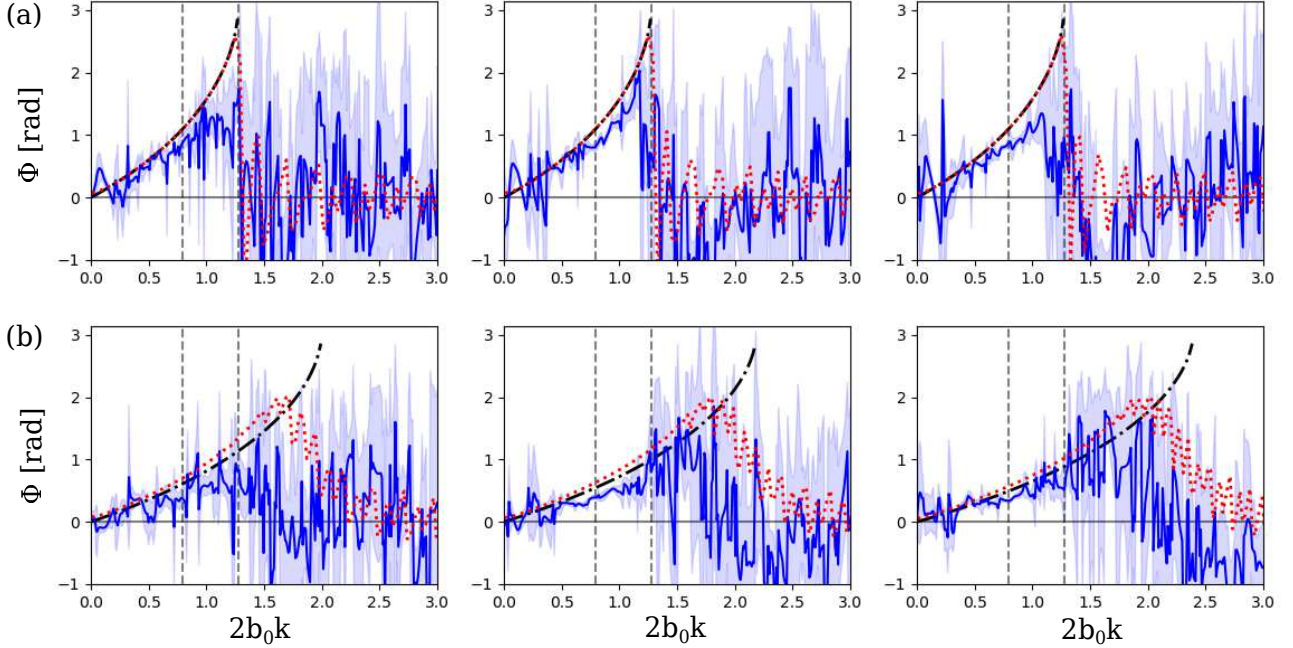
FIG. 11. Measured phase shift between the upper and lower filament boundaries as a function of wavenumber for (a) $\epsilon^* = 0$, $t^* = 22.5, 24.75, 27$; (b) $\epsilon^* = 0.02$, $t^* = 22.5, 27, 31.5$. Also shown are predictions of Eq. (14) where k is scaled by $\exp(\epsilon t)$ (black, dash-dot), and solutions to the linear contour dynamics model [Eq. (12)] averaged over initial phase (red, dotted). Shaded regions indicate the experimental uncertainty, k_m and k_c are indicated (dashed lines), and for $\epsilon^* \neq 0$ instability is predicted for $k < k_c \exp(\epsilon t)$.
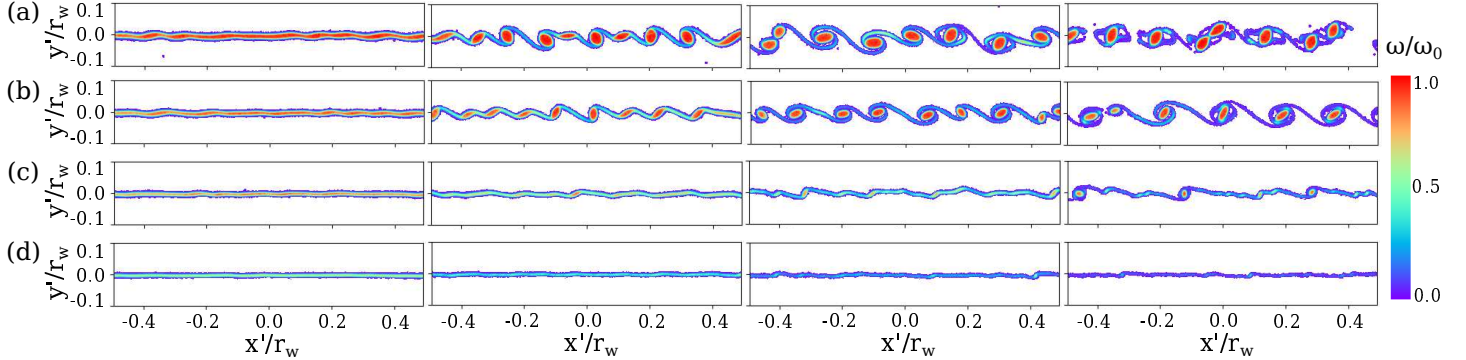

FIG. 12. Measurements of the vorticity ω (color map) for $\epsilon^* =$ (a) 0, (b) 0.015, (c) 0.03, and (d) 0.045 at times $t^* = 22.5$, 33.75, 45, and 56.25 (left to right).

nonlinearity becomes important, as defined by Eq. (17), for the experimental data (error bars) and solutions to Eqs. (12) with initial wave slope $s(0) = 0.01$ (dotted, independent of k) and $s(0) = 0.03b_0 k$ (dashed). Here, the error bars for t^*_{NL} correspond to the time window between the black circles in Fig. 14 and the preceding data point. The curves corresponding to the numerical model terminate when ϵ^* is high enough that Eq. (17) is never satisfied. The linear spectrum of the initial slope $s \propto k$ was chosen to model a constant initial wave amplitude (independent of k), as might be expected due to discrete-particle or finite gyroradius effects. Panel (b) shows the wavenumber k_{NL} for which Eq. (17) is first sat-

isfied, corresponding to t^*_{NL} for the linear model shown in panel (a). Panel (c) shows the spatial scale of the experimental filament $b_{\mathrm{eff}}(t^*_{\mathrm{NL}})$ at the onset of nonlinearity. In both the model and the experiment, the same general trends are observed. However, it appears that the experimental instability reaches nonlinearity at higher values of ϵ^* where the model does not, suggesting that the initial wave slope spectrum might be better described by a nonlinear function of k.

The mean perpendicular profiles of the vorticity distributions are found by integrating over the region of interest, $\langle \omega \rangle_{x'} = r_w^{-1} \int \omega(x', y') \mathrm{d}x'$. They are plotted in Fig. 16 for $\epsilon^* =$ (a) 0, (b) 0.015, and (c) 0.03 at times $t^* =$
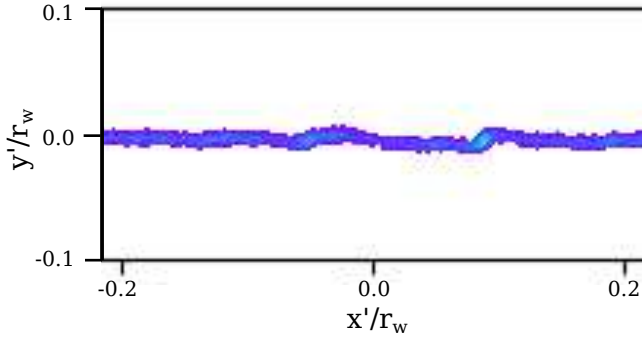
FIG. 13. Enlarged view of the vorticity ω (color map) for $\epsilon^* = 0.045$ at time $t^* = 56.25$ [last panel of Fig. 12(d)], showing evidence of nonlinearity and vortex formation near the pixel resolution of the CCD camera (1 pixel = $2.5 \times 10^{-3} r_w$).
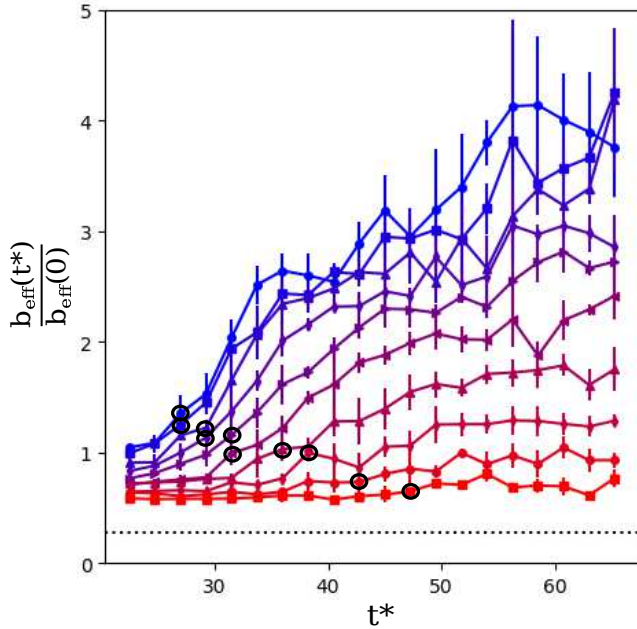

FIG. 14. Evolution of the effective filament width b_{eff} [cf. Eq. (8)] normalized to its initial value for $\epsilon^* = 0 - 0.045$ (blue to red). Black circles indicate the onset of nonlinearity, where Eq. (17) is first satisfied. The value of b_{eff} corresponding to a single pixel is also shown (dotted).

0, 22.5, 31.5, 40.5, 49.5 and 58.5. Gaussian functions are numerically fit to the profiles and shown as dotted lines, which are almost indistinguishable from the experimental data. Thus, as the instability proceeds, the mean profile assumes a nearly Gaussian shape of width b_{eff} which spreads due to both the primary shear instability and the secondary vortex pairing instability. In Fig. 16(a) ($\epsilon^* = 0$), the total circulation is nearly constant, whereas in panels (b,c) ($\epsilon^* \neq 0$) it decreases over time due to advection out of the region of interest by the strain flow.

Data beyond $t^* = 65.25$ are not shown since the time window discussed here encapsulates the physics on which this work focuses. However, a few experimental runs
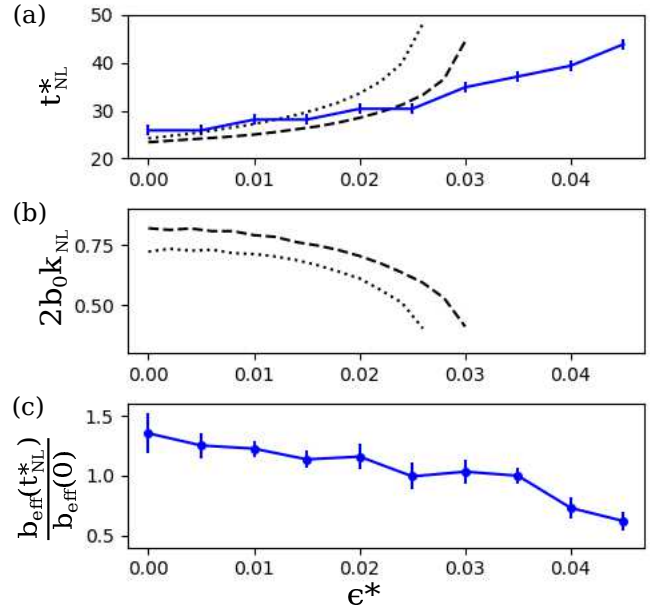

FIG. 15. Measurements (error bars) and predictions of the linear model (black lines) showing (a) the time t^*_{NL} at which nonlinearity becomes important [as defined by Eq. (17)] versus ϵ^*; (b) the wavenumber k_{NL} for which Eq. (17) is first satisfied in the model; and (c) the effective half-width $b_{\text{eff}}(t^*_{\text{NL}})$ at the onset of nonlinearity. The model is averaged over initial phase and plotted for $s(0) = 0.01$ (dotted) and $s(0) = 0.03 b_0 k$ (dashed).

at later times were conducted in order to determine the qualitative behavior. In the absence of strain, the vortices continue to pair and merge. This causes the spacing between vortices to increase, and therefore the timescale for further pairing and merging events increases as well. On long timescales ($t^* \sim 100 - 200$), the entire array of vortices becomes curved due to the influence of image fields. Eventually, the remaining vortices begin to move chaotically around the circular domain, occasionally interacting and/or merging.

In the presence of the external strain flows studied here with $0 \leq \epsilon^* \leq 0.045$, once the vortices have formed they tend to be stable since the strain is much weaker than the Moore-Saffman limit $\epsilon^* \approx 0.15$ at which elliptical patch vortices lose stability.[18,35,37] Thus, after primary saturation, if pairing is suppressed, b_{eff} is expected to be roughly constant. Based on inspection of the vorticity data and the simple point-vortex pairing model described above, it is unlikely that the vortices pair and/or merge for strain rates $\epsilon^* > 0.025$ at times $t^* > 65.25$. In this case, the vortices are advected away from the origin due to the strain and eventually carried out of the region of interest and out of the system through gaps between the segmented electrodes. This behavior is outside the scope of the current study.
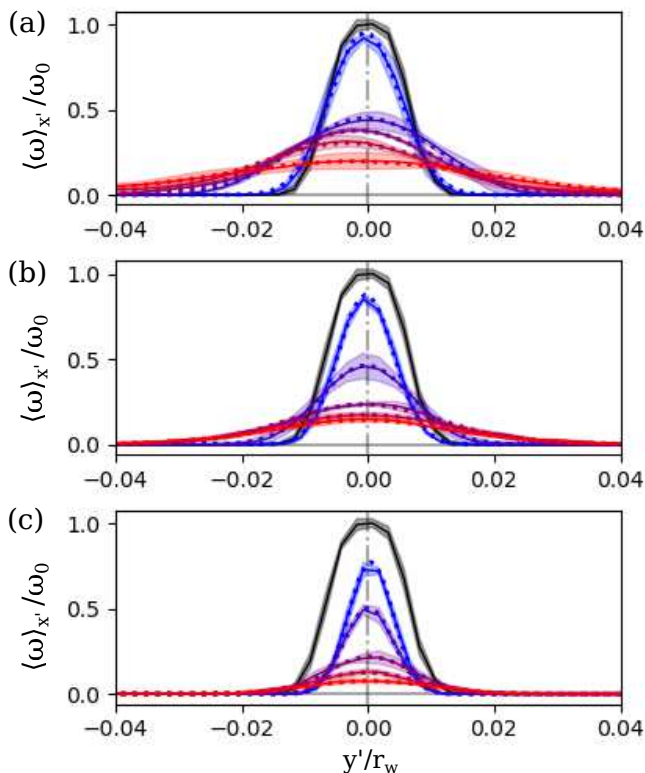
FIG. 16. The mean vorticity profile perpendicular to the filament (i.e., averaged over the x' direction), for $\epsilon^* =$ (a) 0, (b) 0.015, and (c) 0.03, at times $t^* = 0$ (black), 22.5, 31.5, 40.5, 49.5, and 58.5 (blue to red). Solid lines and shaded regions indicate the average and standard deviation of five identical runs. Dotted lines indicate Gaussian fits to the data.

V.   DISCUSSION AND CONCLUSIONS

The experimental studies presented here focus on the linear and nonlinear behavior of $\mathbf{E} \times \mathbf{B}$ shear instabilities in electron plasmas under the influence of applied strain flows. By precisely controlling the boundary conditions on the electrodes in 2D, the electrons can be subjected to externally applied strain flows.[33–35] Here, electron vortices are stretched into thin, rectangular filaments (i.e., $\mathbf{E} \times \mathbf{B}$ shear layers) by applying strong strain flows, and then the strain-to-vorticity ratio is reduced to either zero or a small value $\epsilon^* \leq 0.045$ and the filament evolution is studied. In the absence of strain, the filament is unstable to the Rayleigh shear mechanism,[3,17] causing waves to grow and break. This results in the formation of a linear array of discrete vortex structures, which is then unstable to the vortex pairing mechanism,[24,38] leading to vortex merger events and transport of vorticity perpendicular to the filament.

When the strain rate is nonzero, the filament (approximately aligned with the strain axis) thins over time due to inflow along the perpendicular direction, and developing waves are stretched toward lower wavenumbers due to outflow along the parallel direction. Due to these ef-

fects, which appear as exponential, time-dependent parameters in the equations of motion, the linear dynamics are non-modal. The net result is that waves experience temporary amplification before becoming damped at sufficiently small k.[31] If the amplification is large enough, nonlinearity becomes important and the waves can break and form vortex chains. However, the spacing between the vortices increases over time due to advection by the strain flow; and so, if the strain is sufficiently strong, then the vortex pairing mechanism is suppressed. The overall effect is that perpendicular transport of the vorticity due to the instability is significantly reduced as the strain rate is increased.

In the linear regime, the experimental data are consistent with theoretical results of Rayleigh[3,17] and Dritschel, et. al.[31] using the contour dynamics technique.[18] An important insight is that, in the presence of strain, the phase shift between waves on the upper and lower surface of the filament continuously evolves toward an instantaneous normal-mode configuration[61] which changes over time as the filament thins.

In terms of nonlinear physics, we find that $\epsilon^* \gtrsim 0.025$ is sufficient to suppress the vortex pairing instability, and that $\epsilon^* \gtrsim 0.04$ is sufficient to limit the perpendicular vorticity spread to less than its initial value, although these results may depend on the initial seed wave amplitude. Since evidence of vortex formation was observed near the spatial scale of the pixel resolution of the CCD, no conclusions could be reached regarding the value of ϵ^* for which vortex formation is prevented altogether. It is interesting that the strain rates studied here, $0 \leq \epsilon^* \leq 0.045$, which have a significant effect on the shear instability, are relatively small compared to the Moore/Saffman elliptical vortex stability limit $\epsilon^* \approx 0.15$.[18,37] This implies that the system exhibits hysterisis, in the sense that an external strain flow is much more effective at inhibiting a shear instability than it is at breaking apart an elliptical vortex which has already formed.

Open directions of research include investigating the effect of profile smoothness on the shear instability[19–21] and Love instabilities which grow on highly elliptical vortices,[18,62,63] and further developing theoretical descriptions of the nonlinear regime (e.g., using point-vortex and vortex patch models[22,36] and/or spectral truncation methods[23]). Finally, it would useful to generalize the present results to other more complicated quasi-2D fluid systems of interest to geophysics, astrophysics, and the magnetic fusion community, e.g., potential vorticity models.[4,6,8,52]

[1] D. G. Dritschel and B. Legras, Phys. Today **46:3**, 44 (1993).
[2] R. Salmon (Oxford University Press (New York), 1998).
[3] J. R. Carpenter, E. W. Tedford, E. Heifetz, and G. A. Lawrence, Appl. Mech. Rev. **64:6**, 060801 (2011).
[4] T. E. Dowling, Int. J. Mod. Phys. D **23:4**, 1430006 (2014).
[5] H. Biglari, P. H. Diamond, and P. W. Terry, Phys. Fluids B **2**, 1 (1990).
[6] P. W. Terry, Rev. Mod. Phys. **72:1**, 109 (2000).
[7] E. Kim and P. H. Diamond, Phys. Rev. Lett. **90:18**, 185006 (2003).
[8] R. V. E. Lovelace, H. Li, S. A. Colgate, and A. F. Nelson, Astrophys. Journal **513**, 805 (1999).
[9] Y. Lithwick, Astrophys. Journal **670**, 789 (2007).
[10] P. S. Marcus, S. Pei, C. H. Jiang, J. A. Barranco, P. Hassanzadeh, and D. Lecoanet, Astrophys. J. **808**, 1 (2015).
[11] R. H. Levy, Phys. Fluids **8:7**, 1288 (1965).
[12] A. J. Cerfon, Phys. Rev. Lett. **116**, 174801 (2016).
[13] C. C. Cutler, J. Appl. Phys. **27:9**, 1028 (1956).
[14] G. Rosenthal, G. Dimonte, and A. Y. Wong, Phys. Fluids **30:10**, 3257 (1987).
[15] A. J. Peurrung and J. Fajans, Phys. Fluids **5:2**, 493 (1993).
[16] S. Chen, G. Maero, and M. Rome, J. Plasma Phys. **83:3**, 705830303 (2017).
[17] L. Rayleigh, Proc. Lond. Math Soc. **11**, 57 (1880).
[18] P. G. Saffman (Cambridge University Press, 1992).
[19] R. J. Briggs, J. D. Daugherty, and R. H. Levy, Phys. Fluids **13**, 421 (1970).
[20] A. E. Fraser, M. J. Pueschel, P. W. Terry, and E. G. Zweibel, Phys. Plasmas **25**, 122303 (2018).
[21] J. R. Carpenter and A. Guha, Phys. Fluids **31**, 081701 (2019).
[22] A. Guha, M. Rahmani, and G. A. Lawrence, Phys. Rev. E **87**, 013020 (2013).
[23] A. E. Fraser, P. W. Terry, E. G. Zweibel, and M. J. Pueschel, Phys. Plasmas **24**, 062304 (2017).
[24] W. Dong, E. W. Tedford, M. Rahmani, and G. A. Lawrence, Phys. Rev. Fluids **4**, 063902 (2019).
[25] J. M. Finn, D. del Castillo-Negrete, and D. C. Barnes, Phys. Plasmas **6:10**, 3744 (1999).
[26] J. C. McWilliams, J. Fluid Mech. **219**, 361 (1990).
[27] J. Weiss, Physica D **48**, 273 (1991).
[28] N. K.-R. Kevlahan and M. Farge, J. Fluid Mech. **346**, 49 (1997).
[29] Y. Kawai, Y. Kiwamoto, Y. Soga, and J. Aoki, Phys. Rev. E **75**, 066404 (2007).
[30] D. G. Dritschel, J. Fluid Mech. **206**, 193 (1989).
[31] D. G. Dritschel, P. H. Haynes, M. N. Juckes, and T. G. Shepherd, J. Fluid Mech. **230**, 647 (1991).
[32] C. F. Driscoll and K. S. Fine, Phys. Fluids B **2**, 1359 (1990).
[33] N. C. Hurst, J. R. Danielson, D. H. E. Dubin, and C. M. Surko, Phys. Rev. Lett. **117**, 235001 (2016).
[34] N. C. Hurst, J. R. Danielson, and C. M. Surko, AIP Conf. Proc. **1928**, 020007 (2018).
[35] N. C. Hurst, J. R. Danielson, D. H. E. Dubin, and C. M. Surko, J. Fluid Mech. **848**, 256 (2018).
[36] S. Kida, J. Phys. Soc. Japan **50:10**, 3517 (1981).
[37] D. W. Moore and P. G. Saffman, in *Aircraft wake turbulence and its detection*, edited by M. R. J. H. Olsen, A. Goldburg (Plenum Press, New York, 1971) pp. 339–354.
[38] C. D. Winant and F. K. Browand, J. Fluid Mech. **63:2**, 237 (1974).
[39] T. M. O'Neil, Phys. Today **52:24**, 24 (1999).
[40] R. C. Davidson (Addison-Wesley, Redwood City, CA, 1990).
[41] J. R. Danielson, D. H. E. Dubin, R. G. Greaves, and C. M. Surko, Rev. Mod. Phys. **87:1**, 247 (2015).
[42] D. H. E. Dubin and T. M. O'Neil, Rev. Mod. Phys. **71:1**, 87 (1999).
[43] D. H. E. Dubin, Phys. Plasmas **5:5**, 1688 (1998).
[44] D. H. E. Dubin, Phys. Plasmas **10:5**, 1338 (2003).
[45] J. Aoki, Y. Kiwamoto, Y. Soga, and A. Sanpei, Japanese J. Appl. Phys. **43:10**, 121 (2004).
[46] D. Durkin and J. Fajans, Rev. Sci. Instrum. **70:12**, 4539 (1999).
[47] R. Chu, J. S. Wurtele, J. Notte, A. J. Peurrung, and J. Fajans, Phys. Fluids B **5:7**, 2378 (1993).
[48] J. R. Danielson and C. M. Surko, Phys. Plasmas **13**, 055706 (2006).
[49] H. Aref, Ann. Rev. Fluid Mech. **15**, 345 (1983).
[50] P. Tabeling, Phys. Reports **362**, 1 (2002).
[51] P. J. Morrison, Rev. Mod. Phys. **70:2**, 467 (1998).
[52] A. Hasegawa and K. Mima, Phys. Fluids **21:87**, 87 (1978).
[53] D. Montgomery and L. Turner, Phys. Fluids **23:2**, 264 (1980).
[54] A. Mariotti, B. Legras, and D. G. Dritschel, Phys. Fluids **6:12**, 3954 (1994).
[55] R. R. Trieling, M. Beckers, and G. J. F. V. Heijst, J. Fluid Mech. **345**, 165 (1997).
[56] X. P. Huang, F. Anderegg, E. M. Hollmann, C. F. Driscoll, and T. M. O'Neil, Phys. Rev. Lett. **78:5**, 875 (1997).
[57] E. M. Hollmann, F. Anderegg, and C. F. Driscoll, Phys. Plasmas **7:7**, 2776 (2000).
[58] A. J. Peurrung and J. Fajans, Phys. Fluids B **5:12**, 4295 (1993).
[59] J. M. Kriesel and C. F. Driscoll, Phys. Rev. Lett. **87**, 135003 (2001).
[60] T. M. O'Neil, Phys. Fluids **23:4**, 725 (1980).
[61] A. Guha and G. A. Lawrence, J. Fluid Mech. **755**, 336 (2014).
[62] A. E. H. Love, Proc. London Math. Soc. **25**, 18 (1893).
[63] T. B. Mitchell and L. F. Rossi, Phys. Fluids **20**, 054103 (2008).